Charge carrier coupling to the soft phonon mode in a ferroelectric semiconductor

Mark E. Ziffer, Lucas Huber, Feifan Wang, Victoria A. Posey, Jake C. Russell, Taketo Handa, Xavier Roy, and X.-Y. Zhu*

Department of Chemistry, Columbia University, New York, New York 10027, USA

(Received 17 May 2022; accepted 12 August 2022; published 2 September 2022)

Many crystalline solids possess strongly anharmonic "soft" phonon modes characterized by diminishing frequency as temperature approaches a critical point associated with a symmetry breaking phase transition. While electron–soft phonon coupling can introduce unique scattering channels for charge carriers in ferroelectrics, recent studies on the nonferroelectric lead halide perovskites have also suggested the central role of anharmonic phonons bearing resemblance to soft modes in charge carrier screening. Here we apply coherent phonon spectroscopy to directly study electron coupling to the soft transverse optical phonon mode in a ferroelectric semiconductor SbSI. Photogenerated charge carriers in SbSI are found to be exceptionally long lived and are associated with a transient electro-optical effect that can be explained by interactions between charge carriers and thermally stimulated soft phonon excitations. These results provide strong evidence for the role of electron–soft phonon coupling in the efficient screening of charge carriers and in reducing charge recombination rates, both desirable properties for optoelectronics.

DOI: 10.1103/PhysRevMaterials.6.095401

I. INTRODUCTION

Recent studies have suggested that the interplay between lattice and charge carrier dynamics in strongly anharmonic polar semiconductors, such as lead halide perovskites, could explain their outstanding optoelectronic properties [1–6]. These findings have recently led to a "ferroelectric polaron" proposal, in which electron coupling to polar anharmonic phonon modes bearing resemblance to soft phonons in ferroelectrics may lead to local ordering of dipoles from unit cells with broken symmetry [7,8]. Generally speaking, soft phonons refer to a lattice mode associated with a symmetry-breaking atomic displacement, and exhibit a temperature dependent vibrational frequency diminishing towards zero as a symmetry-breaking phase transition is approached [9–11]. Soft phonons are particularly important in displacive-type ferroelectric crystals, wherein the ferroelectric-paraelectric phase transition is driven by the softening of a phonon mode whose normal coordinate corresponds to atomic displacement along the symmetry-breaking axis of spontaneous polarization [9,12,13]. Historically, electron–soft phonon coupling in ferroelectrics has been studied with regard to phase transitions, where temperature dependent vibrational mixing between electronic bands mediated by a soft phonon mode has been proposed to drive the ferroelectric-paraelectric phase transformation [14,15]. Additionally, electron–soft phonon coupling in ferroelectrics has been studied in wide-band gap ferroelectric crystals such as perovskite oxides to understand the scattering interactions that influence charge carrier mobility and electrical transport [16–20].

For electron-phonon coupling in conventional semiconductors, one is commonly concerned with the long range Fröhlich interaction, which describes the Coulomb interaction between an electron and the macroscopic electric field in the lattice associated with atomic displacement along a polar longitudinal optical (LO) phonon mode [21,22]. However, the soft phonon in ferroelectrics is a transverse optical (TO)–phonon mode according to the Lyddane-Sachs-Teller relation [10,12] and consequently does not give rise to a long range electric field, preventing coupling with electrons via the Fröhlich interaction [8,16]. Instead, electron coupling with soft TO phonons has been addressed by Wemple *et al.* as involving the scattering of charge carriers via the polarization potential interaction [16,23,24], by Nasu and co-workers in the formation of small and large "superparaelectric" polarons [25,26], and by Bernardi and co-workers in the direct charge carrier scattering studied with *ab initio* dynamics [17,18].

Most experimental studies on electron–soft phonon coupling in ferroelectric crystals have relied on analyzing temperature dependent charge transport phenomena [16–20]. These measurements do not directly probe mode-specific electron-phonon interactions, and the involvement of soft phonons often comes from qualitative comparisons to theoretically predicted temperature dependences in mobility. Furthermore, few experiments have directly studied the role of electron–soft phonon coupling in the photophysics of semiconductors, and ferroelectric semiconductors provide an excellent model system to explore such phenomena. Here, we study mode-specific electron-phonon coupling in a ferroelectric semiconductor, SbSI, using ultrafast pump-probe coherent phonon spectroscopy [27–29]. Softening of a TO-phonon mode associated with the ferroelectric phase transition has been studied extensively in SbSI [30–34], and together with an optical band gap in the visible region (∼2.0 eV) [35,36], SbSI

*Corresponding author: xz2324@columbia.edu

serves as an ideal semiconductor for studying electron–soft phonon coupling by pump-probe optical spectroscopy. Using a broadband probe with photon energies across the band gap of SbSI, we directly identify coupling between photoexcited electrons and coherently excited soft phonons. Furthermore, we find evidence from transient reflectance spectroscopy to suggest that charge carrier dynamics in SbSI are strongly influenced by coupling between free charges and thermally stimulated soft phonon excitations, resulting in long charge carrier recombination lifetimes associated with a transient electro-optical effect.

II. METHODS

A. Pump-probe coherent phonon and transient reflectance spectroscopy

The fundamental output of an ultrafast Ti:sapphire regenerative amplifier (Coherent Legend 10 kHz, 5 mJ, seeded by Coherent Vitara oscillator) is split into two paths. One path of the fundamental is frequency doubled in a beta barium borate (BBO) crystal to generate a ∼200-fs pump pulse centered at 3.1 eV, while several μJ from the other path is focused into a sapphire crystal to generate a white light continuum used for the probe pulse (see Supplemental Material Section S4 for time domain characterization of the pump and probe pulses [37]). The polarization of the incident pump and probe pulses is controlled using half wave plates, with an additional linear polarizer used for the probe. Pump and probe pulses are overlapped at near normal incidence on a SbSI crystal mounted in a continuous flow LN_2 cryostat (Oxford MicroStat Hi-Res). Reflected probe light is sent through a linear polarizer with polarization axis set to match the polarization of the incoming probe, and is then dispersed by a 600-g/mm diffraction grating blazed at 500 nm and imaged onto a line-scan charge-coupled device (CCD) camera (e2v AViiVA EM4). The pump pulse is chopped at half the laser repetition rate (5 kHz), and shot-to-shot synchronization with the line-scan camera is controlled by triggering a PCI-e framegrabber (NI PCIe-1433). The pump-probe delay is controlled using a mechanical delay stage in the pump line. The instrumentation is controlled and data recorded with custom written LABVIEW code, from which the pump-on vs pump-off signal of the line-scan camera is used to calculate $\Delta R/R$.

B. Polarization resolved Raman spectroscopy

A 633-nm HeNe laser was used to measure low-frequency Raman scattering on a homemade setup built around a Nikon TE-300 inverted microscope. A half wave plate followed by a linear polarizer fixes the polarization at the HeNe laser source, which is sent to a reflective bandpass filter (Ondax), through a half wave plate mounted on a motorized rotation stage used to control the angle of incident polarization in the sample plane, and into the microscope objective (40X, NA = 0.6). The objective is focused onto an SbSI crystal (the same used for coherent phonon spectroscopy) mounted in a continuous flow LN_2 cryostat (Oxford MicroStat Hi-Res). The backscattered light from the sample is collected through the same objective and sent back through the same motorized half wave plate, which projects the parallel polarized Raman signal onto the polarization axis fixed at the HeNe laser, and the cross polarized Raman signal onto the orthogonal axis. The backscattered signal is then sent through two sets of volumetric Bragg filters (Ondax) to filter out the Rayleigh scattered laser line and the parallel polarized Raman signal is selected using a half wave plate and fixed linear polarizer downstream of the Bragg filters. The Raman signal is focused onto the entrance slit of a spectrometer (Princeton Instruments HRS-300) with a high-resolution holographic grating that disperses the spectrum onto a LN_2 cooled CCD camera (Princeton Instruments LN400/B).

C. SbSI synthesis and characterization

SbSI crystals were synthesized according to a previously published flux reaction [38] with 40 mol % of Sb_2S_3 in SbI_3. The powders were grinded, pressed into a pellet, and placed in a quartz tube. The pellet was melted with a propane torch under ∼1 atm of nitrogen, cooled, and then melted again. Quartz wool was placed approximately halfway down the quartz tube and indents were made above the placement of the wool. The tube was sealed under partial pressure of nitrogen and placed in a box furnace. The reaction was heated to 475 °C over the course of a few hours, left at 475 °C for 2 h, and ramped down to 350 °C at a rate of 0.5 °C/hr. The tube was taken out of the oven while at 350 °C and flipped over to filter the excess starting reagents with the use of the quartz wool. The crystals were washed with boiling methanol to remove leftover SbI_3. The SbSI crystals were characterized using an Agilent SuperNova single crystal x-ray diffractometer and compared to the literature.

III. RESULTS AND DISCUSSION

Soft-mode characterization and electron soft phonon coupling. Single crystal SbSI is a prototypical ferroelectric semiconductor that features a ferroelectric phase transition typically described by a displacive-type mechanism. In this mechanism softening of a ferroelectric TO-phonon mode drives the crystal from a low symmetry C_{2v}^9 ($Pna2_1$) ferroelectric phase to a high symmetry D_{2h}^{16} ($Pnam$) paraelectric phase at ∼288 K [10,30,31,33,35]. We note that several proposals for transitioning to an intermediate phase between 298 and 410 K have also been reported [34,39,40], where the proposed mechanisms [34,41,42] are consistent with models that also show displacive-type phase transition behavior in molecular dynamics simulations [43,44]. Figure 1(a) shows the crystal structure of SbSI in the ferroelectric phase [45] with several unit cells stacked vertically along the crystallographic c axis, which corresponds to the axis of spontaneous polarization [46]. Previous studies have identified the soft mode in SbSI as an IR and Raman active TO phonon involving the displacement of Sb-S atoms along the crystallographic c axis [33]. Polarization resolved Raman scattering measurements and group theory calculations have shown that the soft phonon mode is of A_u symmetry, with a Raman tensor consisting of a dominant α_{zz} component, where z is the coordinate along the c axis [30,33]. We use polarization resolved Raman spectroscopy to first characterize the soft phonon mode in a flux-synthesized single crystal of SbSI. Figure 1(b) shows

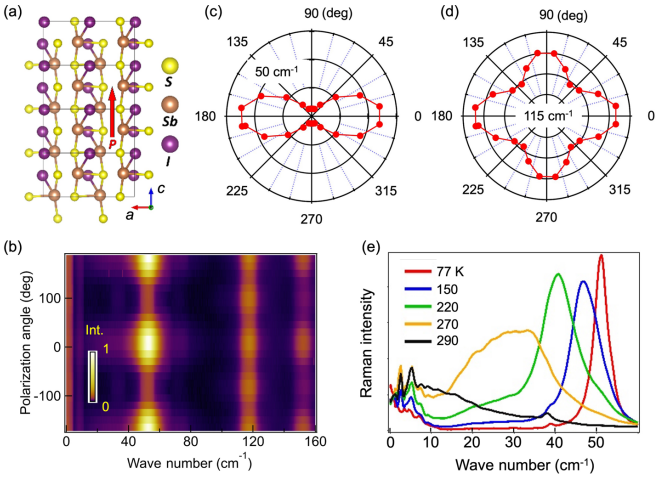

FIG. 1. Raman spectra identifying the soft phonon mode in SbSI. (a) Crystal structure of SbSI in the ferroelectric C_{2v}^9 ($Pna2_1$) phase. The spontaneous polarization is directed along the crystallographic c axis as indicated by the red arrow. (b) Polarization-angle resolved Raman spectrum of SbSI at 80 K with incident polarization in the xz plane ($z = c$ axis, $x = a$ or b axis) and scattered polarization parallel to incident polarization. Color bar indicates the Raman scattering intensity (a.u.) (c),(d) Polar plots corresponding to spectral cuts from (b) integrated around the ∼50 cm^{-1} and ∼115 cm^{-1} modes. (e) Temperature dependence of the parallel polarized Raman scattering showing softening of the 50 cm^{-1} (80 K) phonon mode. We note that the small peak observed at ∼39 cm^{-1} that does not soften with temperature has been characterized previously as a "hard" mode with a different Raman tensor than the ferroelectric soft mode [31,32].

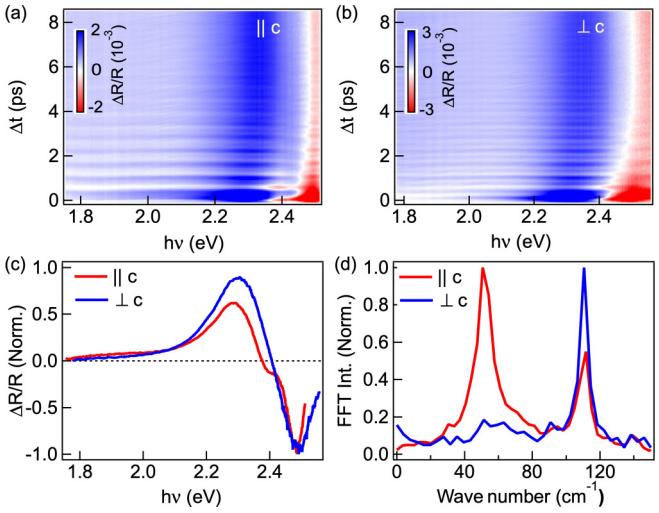

FIG. 2. Coherent phonon spectra of SbSI. (a),(b) Transient reflectivity of SbSI measured at 80 K for probe polarizations parallel and perpendicular to the c axis, respectively. Color bars indicate the magnitude of $\Delta R/R$. (c) Normalized spectral cuts of the transient reflectivity data in (a) and (b) integrated between $\Delta t = 0$ and 0.1 ps. (d) Normalized FFT spectra of the time differentiated transient reflectivity data in (a) and (b), taken from signal transients spectrally integrated in the below-gap region (1.7–1.9 eV).

the polarization resolved Raman spectrum of SbSI measured at 80 K in the backscattering geometry, with incident polarization in the xz plane and signal collected for scattered polarization parallel to the incident polarization. Here x is in the direction of either the a or b axis, which we do not distinguish since the Raman responses for polarization incident in the c-a and c-b planes in SbSI are known to be similar [47]. Figures 1(c) and 1(d) show polar plots for the polarization dependent Raman signal taken from cuts along the two dominant modes at ∼50 and ∼115 cm^{-1} in Fig. 1(b). Both the frequency and the symmetry for the parallel polarized Raman scattering of the 50-cm^{-1} mode at 80 K are in good agreement with those of the ferroelectric soft mode identified in previous experiments [30,33]. The polarization dependence of the 115-cm^{-1} mode, which does not soften with temperature, is also in good agreement with previous studies [30]. Figure 1(e) confirms the characterization of phonon softening for the 50-cm^{-1} mode identified at 80 K, shown by the decrease in vibrational frequency when the sample temperature is increased towards the ferroelectric phase transition temperature at ∼290 K [37]. Furthermore, the broadening of the soft-mode Raman spectrum with temperature and appearance of a central-peak towards zero wave number at ∼290 K [Figure 1(e)] are clear indications of temperature dependent anharmonic phonon-phonon interactions that dampen the vibrational resonance and drive phonon softening in displacive ferroelectric crystals [10,32]. We also verify the trend of the ferroelectric phase transition by measuring the temperature dependence of the optical second harmonic generation intensity (see Supplemental Material Fig. S5 [37]), and observe a phase transition temperature of ∼290 K.

To study electron-phonon coupling with the soft mode, we use ultrafast pump-probe coherent phonon spectroscopy. We excite SbSI above the band gap using a ∼200-fs laser pulse centered at $h\nu_1 = 3.1$ eV (15 $\mu J/cm^2$), with pump polarization parallel to the c axis. The pump bandwidth is sufficiently broad to stimulate a wave packet of coherent phonons with frequencies up to ∼165 cm^{-1} via the nonlinear impulsive stimulated Raman mechanism [48–50]. Figures 2(a) and 2(b) show the near-normal incidence transient reflectivity spectrum ($\Delta R/R$) of SbSI at 80 K probed by a ∼100-fs broadband probe pulse ($h\nu_2 \sim 1.75$–2.5 eV) polarized either parallel or perpendicular to the crystallographic c axis. The pump-induced phonon wave packet modulates the complex optical susceptibility of SbSI, which results in coherent oscillations in the reflectivity ($\Delta R/R$) [48]. To confirm that the coherent phonons come from the same modes characterized in Raman scattering, we analyze the below-gap coherent phonon response, which corresponds to modulation of the real part of the optical response due to the Raman susceptibility tensor [48]. Figure 2(c) shows spectral cuts of the pump-probe data from Figs. 2(a) and 2(b) around time zero, showing derivative-like features from $h\nu_2 \sim 2.1$–2.5 eV that can be attributed to an electronic response from SbSI due to the above-gap pump energy [46,51]. At $h\nu_2 < 2.0$ eV, the transient reflectance spectrum stays flat at $\Delta R/R \sim 0$, which is consistent with low temperature absorption measurements on SbSI showing that the lowest energy indirect absorption edge lies above 2.0 eV at 80 K [52]. We therefore assign the spectral range at $h\nu_2 \leqslant 1.9$ eV to signal dominated by the below-gap coherent phonon response.

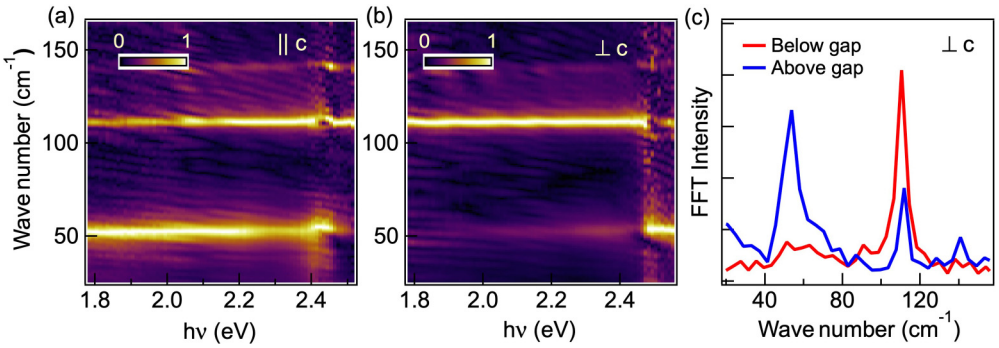

FIG. 3. Evidence for electron–soft phonon coupling in the above-gap probe of coherent phonons. (a),(b) Probe $h\nu$-resolved FFT of the coherent phonon signal for probe polarizations parallel (a) and perpendicular (b) to the c axis. FFT spectra are amplitude normalized at each probe frequency and color bars indicate the normalized FFT intensity. (c) Comparison of the FFT of the coherent phonon signal for probe frequencies below and above the band gap in the probe-$\perp c$ polarization geometry. The below-gap FFT is from the coherent phonon signal spectrally integrated between 1.7 and 1.9 eV and the above-gap FFT is from signal spectrally integrated from 2.49–2.56 eV.

In Fig. 2(d) we show the below-gap coherent phonon spectrum for probe-$||c$ and -$\perp c$ polarization geometries, obtained by taking the fast Fourier transform (FFT) of the time differentiated transient reflectance signal ($\frac{d}{dt}\Delta R/R$) from Figs. 2(a) and 2(b) and spectrally integrating for $h\nu_2 \leqslant 1.9$ eV (see Supplemental Material Sec. S7 for further details on FFT analysis [37]). A coherent phonon at 50 ± 2 cm^{-1} modulates the optical response only for probe polarization parallel to the c axis, which is consistent with the symmetry of the Raman tensor for the ferroelectric soft mode identified from Raman scattering [Fig. 1(c)]. Additionally, we note that the coherent phonon at 115 ± 2 cm^{-1} is detected in both probe-$||c$ and probe-$\perp c$ polarization geometries, also in agreement with the polarization dependence of the Raman scattering data [Fig. 1(d)]. Furthermore, we find that the dephasing lifetime of coherent oscillations from the soft mode in the probe-$||c$ polarization decreases as the sample temperature increases from 80 to 270 K (Supplemental Material Sec. S1 [37]), consistent with softening of this phonon mode as the ferroelectric phase transition is approached [10]. In particular, we find that at 270 K coherent oscillations from the soft phonon mode dephase on a time scale around ∼1 ps (Supplemental Material Fig. S1c [37]), corresponding to a resonance linewidth of ∼30 cm^{-1} that is in good agreement with the approximate linewidth of the soft-mode peak observed in Raman scattering at 270 K [Fig. 1e)]. Both the polarization and temperature dependent analysis of the below-gap coherent phonon signal thus provide conclusive evidence that the impulsively stimulated coherent 50 cm^{-1} (80 K) mode corresponds to the ferroelectric soft mode.

We next turn to analyze the coherent phonon response for probe frequencies above the band gap. Figures 3(a) and 3(b) show the $h\nu_2$ resolved FFT spectra of the coherent phonon signal from Figs. 2(a) and 2(b) for probe polarizations parallel and perpendicular to the c axis, respectively, with the FFT amplitude normalized at each probe energy. In the probe-$||c$ polarization geometry [Fig. 3(a)], both the 50- and 115-cm^{-1} modes are observed for $h\nu_2$ below and above the band gap, consistent with the polarization dependence of the Raman susceptibility for these modes. However, in the probe-$\perp$ c geometry [Fig. 3(b)], while the 50-cm^{-1} soft mode is nearly absent at $h\nu_2$ below gap, it is switched on to become dominant above gap at $h\nu_2 \geqslant 2.47$ eV [Fig. 3(b)]. In Fig. 3(c), we highlight the difference between the above-gap and below-gap responses for the probe-$\perp$ c geometry by comparing the FFT spectra integrated in the 1.7–1.9-eV range with that in the 2.49–2.56-eV range. The switching on of coherent oscillations from the soft mode for $h\nu_2$ above the band gap in the Raman symmetry forbidden $E\perp$ c probe polarization geometry can be attributed to the modulation of the optical susceptibility by electron-phonon coupling [22,28,53]. Atomic displacement along a phonon normal coordinate results in a change in the single particle band energies [28], causing a strong modulation of the optical transitions that can be observed in the above-gap optical response in coherent phonon spectroscopy [28,54]. Such mechanisms are analogous to electron-phonon coupling effects in resonance Raman scattering that are responsible for the observation of symmetry forbidden Raman modes in above-band-gap Raman scattering [22,53]. In ferroelectrics, a change in the band energies due to atomic displacement along the soft phonon mode coordinate is described by the polarization potential interaction [16,46], and this mechanism has been used to describe resonant electron–soft phonon coupling effects in Raman scattering in ferroelectric perovskite oxides [55,56]. Based on calculations showing that the second order nonlinear optical coefficient in SbSI is strongly peaked at the lowest energy direct band gap [57], we can also expect coherent oscillations in the optical response due to the polarization potential interaction to be peaked at the lowest energy direct gap due to the direct correspondence between the polarization potential interaction and the nonlinear optical coefficients in ferroelectric materials [12,58]. Thus, the strong modulation of the optical susceptibility due to the soft mode that we observe in the above-gap coherent phonon data [Figs. 3(b) and 3(c)] at the energy of the lowest direct gap measured for SbSI with $E\perp c$ at low temperature [59,60] provides direct evidence for electron–soft phonon coupling.

Charge carrier recombination. We now study charge carrier dynamics using the same pump-probe scheme as in Figs. 2 and 3, but on longer time scales ($\Delta t \leqslant 3$ ns, limited experimentally by the delay stage length). Figure 4(a) shows the transient reflectance data at 270 K in the probe-$\perp$ c polarization geometry. On the nanosecond time scale, the transient

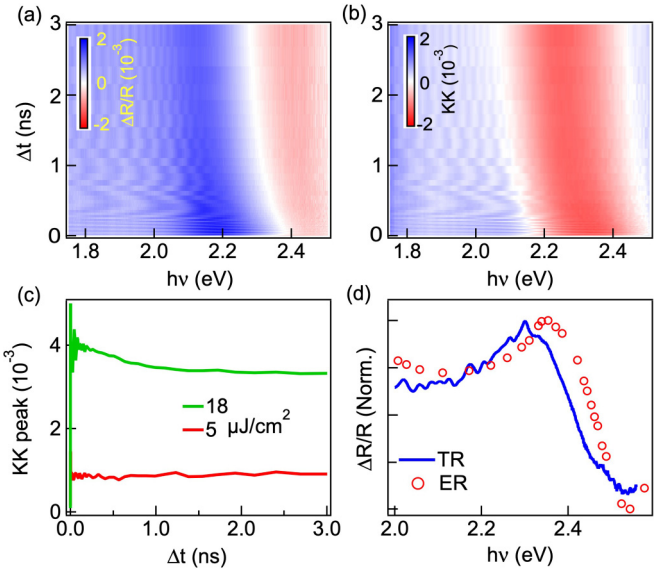

FIG. 4. Dynamics of charge carriers from transient reflectance. (a) Transient reflectance ($\Delta R/R$, color scale) of SbSI at 270 K with probe polarization perpendicular to the c axis. (b) Kramers-Kronig (KK) transform of the data in (a), which gives an approximation to change in the extinction coefficient Δk (color scale). (c) Peak of the KK transformed signal as a function of Δt at excitation pulse energies of $\rho = 5$ μJ/cm^2 (red) 18 μJ/cm^2 (green). (d) Comparison between the transient reflectance spectrum measured at 80 K (integrated for $\Delta t = 0.5$–3 ns for, $\rho = 15$ μJ/cm^2; see Supplemental Material Fig. S3 [37]) for probe $\perp c$ and the electroreflectance spectrum for probe $\perp c$ at 90 K reported previously [60].

reflectance signal above the band gap is typically dominated by changes in the refractive index (Δn) due to the electronic response, which can be approximately converted to a change in extinction coefficient (Δk) via a Kramers-Kronig (KK) transformation [Fig. 4(b)] [51]. The KK transformed transient reflectance data show a long-lived Gaussian-like peak centered around 2.3 eV [Fig. 4(b)], corresponding to the lowest energy direct-gap transition in SbSI [35,46]. Figure 4(c) plots the amplitude of this Gaussian peak in the KK transformed signal as a function of Δt at two excitation pulse energy densities, $\rho = 5$ and 18 μJ/cm^2. At a low excitation density of $\rho = 5$ μJ/cm^2, there is no measurable decay, indicating that the electronic process associated with this feature has a characteristic lifetime more than one order of magnitude longer than the 3-ns experimental limit. Only at the much higher excitation density of $\rho = 18$ μJ/cm^2 do we observe a measurable decay on the subnanosecond time scale, which could be attributed to many-body effects such as Auger recombination of photocarriers [61]. We note that the Gaussian feature in the KK transformed data at 2.3 eV lies well above the indirect gap of SbSI at ~2.0 eV at 80 K [52], suggesting that the transient reflectance spectrum does not simply correspond to a ground state bleach of the lowest energy optical transition.

Interestingly, Fig. 4(d) shows good agreement between the transient reflectance spectrum measured at 80 K with the electroreflectance spectrum of SbSI measured by Zametin *et al.* [60] at 90 K in the same polarization geometry. The transient reflectance spectrum at 270 K is also in good agreement with an electroreflectance effect in SbSI (see Supplemental Material Sec. S2 [37]). We propose that the observation of an electro-optical response associated with photoexcited charge carrier dynamics at 270 K could be explained based on the electron–soft phonon coupling model proposed by Wemple *et al.* [16], which considers coupling between charge carriers and fluctuations in the local ferroelectric polarization caused by thermally stimulated soft phonon excitations. Here, correlated fluctuations in the local ferroelectric polarization [$P_{\rm fluc}(\boldsymbol{r}) = [P(\boldsymbol{r}) - P_0]$, where $P(\boldsymbol{r})$ and P_0 are the local and equilibrium values, respectively, of the polarization at temperature T] can be described in terms of the spectral density of thermally stimulated soft phonon excitations ($\langle|P_q|^2\rangle$) using the general thermodynamic Landau theory [62,63]:

$$\langle P_{\rm fluc}(0)P_{\rm fluc}(\boldsymbol{r})\rangle \propto \sum_q \langle|P_q|^2\rangle e^{i\boldsymbol{qr}}, \tag{1}$$

$$\langle|P_q|^2\rangle \propto \frac{k_B T}{\omega_q^2}. \tag{2}$$

The finite spatial correlation length of polarization fluctuations in Eq. (1) describes "polarization clusters" [16] with nonzero polarization gradients at their boundaries, resulting in corresponding surface bound polarization charge [$\nabla P_{\rm fluc}(\boldsymbol{r}) = \sigma_b$] and local depolarization fields [$E_d(\boldsymbol{r})$] [12,16]. Following above-gap photoexcitation, free charge carriers neutralize the surface bound charge, resulting in a partial screening of a local depolarization field [$\delta E_d(\boldsymbol{r})$], which causes a correlated change in the mean local polarization at [$\delta\langle P(0)\rangle$] according to Landau theory [62,63]:

$$\delta\langle P(0)\rangle = (k_B T)\int \langle P_{\rm fluc}(0)P_{\rm fluc}(\boldsymbol{r})\rangle \delta E_d(\boldsymbol{r})d\boldsymbol{r}. \tag{3}$$

Such spatially correlated changes in polarization due to the screening of cluster depolarization fields will cause a modulation of the band energies near the lowest energy direct gap in SbSI due to the large polarization potential at the lowest energy direct gap noted earlier. This interaction is analogous to the electro-optical effect in ferroelectrics [23,46,60], and can explain the shift in optical transition energies at the direct gap in SbSI that is seen in both the electroreflectance and transient reflectance spectroscopy [Fig. 4(d)]. We note that dynamic changes in lattice polarization due to the screening of bound polarization charge by photoexcited free carriers have been observed directly in ferroelectric $PbTiO_3$ by Lindenberg and co-workers in ultrafast time resolved optical-pump x-ray scattering-probe experiments [64]. The resulting effect of localization of photogenerated electrons and holes at the sites of bound polarization charge will be a screening of the charge-carrier Coulomb potential [7], which can explain the long-lived charge carrier dynamics observed in SbSI near room temperature (270 K).

While interactions between charge carriers and static domains in ferroelectrics are expected to influence charge carrier dynamics [65–68], here we propose that the slow recombination dynamics and associated spectral response at 270 K also reflect the interaction of charge carriers with spatially correlated polarization fluctuations [Eq. (1)]. Evidence for this proposal can be seen in the temperature dependent

Raman spectrum of the ferroelectric soft mode. According to Landau theory, the local polarization correlation function is also described in terms of a characteristic correlation length ξ [62,63]:

$$\langle P_{\text{fluc}}(0)P_{\text{fluc}}(\boldsymbol{r})\rangle \propto k_B T \frac{e^{-|\boldsymbol{r}|/\xi}}{|\boldsymbol{r}|}, \tag{4}$$

$$\xi \propto \frac{1}{\omega_0(T)}. \tag{5}$$

Equations (4) and (5) show that as the ferroelectric soft-mode resonance begins to show a sharp decrease in frequency with temperature approaching the ferroelectric phase transition, we can expect the long-range correlations in polarization fluctuations to become stronger [62]. In terms of charge carrier–soft phonon interactions, this means that the probability for a photoexcited charge carrier to encounter a local polarization fluctuation at any point in space will become large as ξ begins to diverge. In Fig. S6b (Supplemental Material [37]) we plot the trend of the correlation length ξ with temperature based on the shift of the soft phonon Raman peak and find that indeed 270 K appears to mark the onset of a divergence in ξ, indicating an onset of strong long-range correlations in polarization fluctuations [62]. Furthermore, we show in Figs. S6c and S6d (Supplemental Material [37]) that the anomalous peak shape and low energy broadening of the soft-mode Raman peak at 270 K is due to the coupling between the soft phonon mode and a central peak mode based on a central-mode coupled oscillator model [32,69]. The appearance of a central peak mode in ferroelectric phase transitions has been shown to be related to the formation and dynamics of polarization clusters [44,70,71], and has also been studied in SbSI previously [32,42,72].

Raman spectra of the soft phonon mode suggest that 270 K marks the onset of a temperature at which the formation of polarization clusters [16] will appear. Here, a charge carrier interacting with fluctuating polarization clusters and domains [73,74], as described by Wemple *et al.* [16,44], becomes a significant addition to the expected interaction with static domains. The fact that coherent oscillations of the soft phonon can still be observed at 270 K in coherent phonon spectroscopy (Fig. S1, Supplemental Material [37]) suggests that the soft phonon mode is not overdamped at this temperature and polar lattice fluctuations from phonon thermal excitation [Eq. (1)] remains a proper description [44]. As the phase transition temperature is further approached and the soft phonon mode becomes overdamped, a soft "phonon" picture may no longer be appropriate for describing the lattice dynamics, and lattice fluctuations become better described in terms of fluctuating polar nanodomains [3,44]. Such nanoscale polarization fluctuations have been directly observed in ferroelectric materials close to the ferroelectric phase transition temperature using techniques such as x-ray photon correlation spectroscopy [73–77]. Detailed correlation of static and dynamic polar domain structure with μs-ms time scale charge carrier recombination dynamics in SbSI as a function of temperature will be the subject of future study.

IV. CONCLUSION

We have studied electron–soft phonon coupling and charge carrier dynamics in a ferroelectric semiconductor SbSI. By comparing polarization and probe-photon energy resolved coherent phonon spectra with corresponding Raman scattering spectra, we provide direct, mode-specific experimental evidence for electron–soft phonon coupling. Furthermore, we discover exceptionally long-lived charge carrier dynamics associated with a transient electro-optical effect, which can be explained based on charge carrier interactions with thermally stimulated soft phonon excitations. These findings provide insights into the photophysics of ferroelectric semiconductors and support the proposal that electron–soft phonon interactions can be harnessed to provide efficient charge carrier screening, leading to long charge carrier lifetimes in semiconductors [7].

ACKNOWLEDGMENTS

This work was supported by the Vannevar Bush Faculty Fellowship through the Office of Naval Research through Grant No. N00014-18-1-2080. Synthesis of the SbSI single crystal was supported by the Materials Science and Engineering Research Center (MRSEC) through NSF Grant No. DMR-2011738. L.H. acknowledges support from the Swiss National Science Foundation under Project ID 187996. M.E.Z. acknowledges postdoctoral fellowship support from the U.S. Department of Energy Office of Energy Efficiency and Renewable Energy administered by the Oak Ridge Institute for Science and Education (ORISE) for the DOE. ORISE is managed by Oak Ridge Associated Universities (ORAU) under DOE Contract No. DE-SC0014664. All opinions expressed in this paper are the authors' and do not necessarily reflect the policies and views of DOE, ORAU, or ORISE. V.A.P. is supported by the National Science Foundation Graduate Research Fellowship Program (NSF GRFP No. 2019279091). J.C.R. was supported by the U.S. Department of Defense through the National Defense Science & Engineering Graduate Fellowship (NDSEG) Program. We thank Y. Li for assisting with optical second harmonic generation (SHG) measurements.

[1] T. Lanigan-Atkins, X. He, M. J. Krogstad, D. M. Pajerowski, D. L. Abernathy, G. Xu, Z. Xu, D. Y. Chung, M. G. Kanatzidis, S. Rosenkranz *et al.*, Two-dimensional overdamped fluctuations of the soft perovskite lattice in CsPbBr3, Nat. Mater. **20**, 977 (2021).

[2] T. Debnath, D. Sarker, H. Huang, Z. K. Han, A. Dey, L. Polavarapu, S. v Levchenko, and J. Feldmann, Coherent vibrational dynamics reveals lattice anharmonicity in organic-inorganic halide perovskite nanocrystals, Nat. Commun. **12**, 2629 (2021).

[3] O. Yaffe, Y. Guo, L. Z. Tan, D. A. Egger, T. Hull, C. C. Stoumpos, F. Zheng, T. F. Heinz, L. Kronik, M. G. Kanatzidis *et al.*, Local Polar Fluctuations in Lead Halide Perovskite Crystals, Phys. Rev. Lett. **118**, 136001 (2017).

[4] Y. Guo, O. Yaffe, T. D. Hull, J. S. Owen, D. R. Reichman, and L. E. Brus, Dynamic emission stokes shift and liquid-like dielectric solvation of band edge carriers in lead-halide perovskites, Nat. Commun. **10**, 1175 (2019).

[5] A. C. Ferreira, S. Paofai, A. Létoublon, J. Ollivier, S. Raymond, B. Hehlen, B. Rufflé, S. Cordier, C. Katan, J. Even *et al.*, Direct evidence of weakly dispersed and strongly anharmonic optical phonons in hybrid perovskites, Commun. Phys. **3**, 48 (2020).

[6] H. Seiler, S. Palato, C. Sonnichsen, H. Baker, E. Socie, D. P. Strandell, and P. Kambhampati, Two-dimensional electronic spectroscopy reveals Liquid-like lineshape dynamics in CsPbI3 perovskite nanocrystals, Nat. Commun. **10**, 4962 (2019).

[7] K. Miyata and X. Y. Zhu, Ferroelectric large polarons, Nat. Mater. **17**, 379 (2018).

[8] F. Wang, Y. Fu, M. E. Ziffer, Y. Dai, S. F. Maehrlein, and X. Y. Zhu, Solvated electrons in solids-ferroelectric large polarons in lead halide perovskites, J. Am. Chem. Soc. **143**, 5 (2021).

[9] P. A. Fleury, The effects of soft modes on the structure and properties of materials, Annu. Rev. Mater. Sci. **6**, 157 (1976).

[10] J. F. Scott, Soft-mode spectroscopy: Experimental studies of structural phase transitions, Rev. Mod. Phys. **46**, 83 (1974).

[11] S. P. Rudin, Generalization of soft phonon modes, Phys. Rev. B **97**, 134114 (2018).

[12] M. E. Lines and A. M. Glass, *Principles and Applications of Ferroelectrics and Related Materials* (Oxford University Press, Oxford, 1977).

[13] P. Chandra, P. B. Littlewood, C. E. Ascheron, and W. Skolaut, A landau primer for ferroelectrics, in *Physics of Ferroelectrics*, edited by K. M. Rabe, C. H. Ahn, and J.-M. Triscone (Springer-Verlag GmbH, Heidelberg, 2007), pp. 69–116.

[14] N. Kristoffel and P. Konsin, Pseudo-Jahn-Teller effect and second order phase transitions in crystals, Phys. Status Solidi B **21**, K39 (1967).

[15] P. Konsin, Structural phase transitions of antiferroelectric and displacive modulated types caused by electron-phonon interaction, Phys. Status Solidi B **86**, 57 (1978).

[16] S. H. Wemple, M. DiDomenico, and A. Jayaraman, Electron scattering in perovskite-oxide ferroelectric semiconductors, Phys. Rev. **180**, 547 (1969).

[17] J.-J. Zhou and M. Bernardi, Predicting charge transport in the presence of Polarons: The beyond-Quasiparticle regime in $SrTiO_3$, Phys. Rev. Research **1**, 033138 (2019).

[18] J.-J. Zhou, O. Hellman, and M. Bernardi, Electron-Phonon Scattering in the Presence of Soft Modes and Electron Mobility in $SrTiO_3$ Perovskite from First Principles, Phys. Rev. Lett. **121**, 226603 (2018).

[19] W. X. Zhou, J. Zhou, C. J. Li, S. W. Zeng, Z. Huang, H. J. Harsan Ma, K. Han, Z. S. Lim, D. Y. Wan, L. C. Zhang *et al.*, Electron–Soft phonon scattering in *n*-Type $SrTiO_3$, Phys. Rev. B **94**, 195122 (2016).

[20] T. Imaseki and W. Kinase, Electron-scattering model in perovskite oxide ferroelectric semiconductors, Phys. Rev. B **27**, 1228 (1983).

[21] D. Emin, *Polarons* (Cambridge University Press, Cambridge, UK, 2013).

[22] P. Y. Yu and M. Cardona, *Fundamentals of Semiconductors*, 4th ed. (Springer, Heidelberg, 2010).

[23] J. D. Zook and T. N. Casselman, Electro-Optic Effects in Paraelectric Perovskites, Phys. Rev. Lett. **17**, 960 (1966).

[24] R. Resta and D. Vanderbilt, Theory of polarization: A modern approach, in *Physics of Ferroelectrics: A Modern Perspective*, edited by K. M. Rabe, C. H. Ahn, and J.-M. Triscone (Springer, Berlin, 2007), pp. 31–68.

[25] K. Nasu, Photogeneration of superparaelectric large polarons in dielectrics with soft anharmonic T_{1u} phonons, Phys. Rev. B **67**, 174111 (2003).

[26] Y. Qiu, C. Q. Wu, and K. Nasu, Dual electron-phonon coupling model for gigantic photoenhancement of the dielectric constant and electronic conductivity in $SrTiO_3$, Phys. Rev. B **72**, 224105 (2005).

[27] M. Hase, M. Kitajima, A. M. Constantinescu, and H. Petek, The birth of a quasiparticle in silicon observed in time-frequency space, Nature (London) **426**, 51 (2003).

[28] F. Thouin, D. A. Valverde-Chavez, C. Quarti, D. Cortecchia, I. Bargigia, D. Beljonne, A. Petrozza, C. Silva, and A. R. Srimath Kandada, Phonon coherences reveal the polaronic character of excitons in two-dimensional lead halide perovskites, Nat. Mater. **18**, 349 (2019).

[29] L. Luer, C. Gadermaier, J. Crochet, T. Hertel, D. Brida, and G. Lanzani, Coherent phonon dynamics in semiconducting carbon nanotubes: A Quantitative Study of Electron-Phonon Coupling, Phys. Rev. Lett. **102**, 127401 (2009).

[30] D. K. Agrawal and C. H. Perry, Long-wavelength optical phonons and phase transitions in SbSI, Phys. Rev. B **4**, 1893 (1971).

[31] G. Harbeke, E. F. Steigmeier, and R. K. Wehner, Soft phonon mode and mode coupling in SbSI, Solid State Commun. **8**, 1765 (1970).

[32] E. F. Steigmeier, H. Auderset, and G. Harbeke, The central peak in SbSI, Phys. Status Solidi B **70**, 705 (1975).

[33] M. Balkanski, M. K. Teng, S. M. Shapiro, and M. K. Ziolkiewicz, Lattice modes and phase transition in SbSI, Phys. Status Solidi B **44**, 355 (1971).

[34] A. Audzijonis, J. Grigas, A. Kajokas, S. Kvedaravičius, and V. Paulikas, Origin of ferroelectricity in SbSI, Ferroelectrics **219**, 37 (1998).

[35] D. Amoroso and S. Picozzi, *Ab initio* approach to structural, electronic, and ferroelectric properties of antimony sulphoiodide, Phys. Rev. B **93**, 214106 (2016).

[36] K. Žičkus, A. Audzijonis, J. Batarunas, and A. Šileika, The fundamental absorption edge tail of ferroelectric SbSI, Phys. Status Solidi B **125**, 645 (1984).

[37] See Supplemental Material at http://link.aps.org/supplemental/10.1103/PhysRevMaterials.6.095401 for additional results and analysis of coherent phonon, transient reflectance, and Raman scattering spectroscopy; characterization of the ferroelectric phase transition via optical second harmonic generation; time domain pulse characterization for pump-probe spectroscopy; and additional details about data analysis; it also includes Refs. [78–84].

[38] K. Nassau, J. W. Shiever, and M. Kowalchik, The growth of large SbSI crystals: Control of needle morphology, J. Cryst. Growth **7**, 237 (1970).

[39] A. Audzijonis, R. Sereika, and R. Žaltauskas, Antiferroelectric phase transition in SbSI and SbSeI crystals, Solid State Commun. **147**, 88 (2008).

[40] K. Łukaszewicz, A. Pietraszko, and M. Kucharska, Diffuse Scattering, short range order and nanodomains in the paraelectric SbSI, Ferroelectrics **375**, 170 (2008).

[41] A. Audzijonis, S. Kvedaravičius, V. Paulikas, J. Siroicas, N. Mykolaitienė, and R. Šadžius, Origin of optical anomalies in the ferroelectric phase transition region of SbSI and SbSBr crystals, Ferroelectrics **215**, 221 (1998).

[42] J. W. Flocken, R. A. Guenther, J. R. Hardy, and L. L. Boyer, A double well oscillator model for the ferroelectric phase transition in SbSI, Ferroelectrics **135**, 309 (1992).

[43] W. C. Kerr, A. M. Hawthorne, R. J. Gooding, A. R. Bishop, and J. A. Krumhansl, First-order displacive structural phase transitions studied by computer simulation, Phys. Rev. B **45**, 7036 (1992).

[44] T. Schneider and E. Stoll, Molecular-Dynamics study of a three-dimensional one-component model for distortive phase transitions, Phys. Rev. B **17**, 1302 (1978).

[45] SbSI Crystal Structure: Datasheet from "PAULING FILE Multinaries Edition –2012" in *Springer Materials*, edited by P. Villars and K. Cenzual (https://Materials.Springer.Com/Isp/Crystallographic/Docs/Sd_0383413).

[46] K. Nako and M. Balkanski, Electronic band structures of SbSI in the para- and ferroelectric phases, Phys. Rev. B **8**, 5759 (1973).

[47] C. H. Perry and D. K. Agrawal, The raman spectrum of ferroelectric SbSI, Solid State Commun. **8**, 225 (1970).

[48] T. E. Stevens, J. Kuhl, and R. Merlin, Coherent phonon generation and the two stimulated raman tensors, Phys. Rev. B **65**, 144304 (2002).

[49] D. M. Riffe and A. J. Sabbah, Coherent excitation of the optic phonon in Si: Transiently stimulated raman scattering with a finite-lifetime electronic excitation, Phys. Rev. B **76**, 085207 (2007).

[50] J. J. Li, J. Chen, D. A. Reis, S. Fahy, and R. Merlin, Optical probing of Ultrafast Electronic Decay in Bi and Sb with Slow Phonons, Phys. Rev. Lett. **110**, 047401 (2013).

[51] K. Miyata, D. Meggiolaro, M. T. Trinh, P. P. Joshi, E. Mosconi, S. C. Jones, F. de Angelis, and X. Y. Zhu, Large polarons in lead halide perovskites, Sci. Adv. **3**, e1701217 (2017).

[52] A. K. Zeinally, A. M. Mamedov, and S. M. Efendiev, a study of the SbSI absorption edge, Ferroelectrics **6**, 119 (1973).

[53] P. F. Williams and S. P. S. Porto, Symmetry-forbidden resonant raman scattering in Cu_2O, Phys. Rev. B **8**, 1782 (1973).

[54] A. T. N. Kumar, F. Rosca, A. Widom, and P. M. Champion, Investigations of amplitude and phase excitation profiles in femtosecond coherence spectroscopy, J. Chem. Phys. **114**, 701 (2001).

[55] S. H. Wemple and M. DiDomenico, in *Raman Scattering from the Soft Optic Mode in Ferroelectric Crystals, in Light Scattering Spectra of Solids*, edited by G. B. Wright (Springer, New York, 1969), pp. 65–74.

[56] I. P. Kaminow and W. D. Johnston, Quantitative determination of sources of the electro-optic effect in $LiNbO_3$ and $LiTaO_3$, Phys. Rev. **160**, 519 (1967).

[57] H. Akkus and A. M. Mamedov, Linear and nonlinear optical properties of SbSI: First-principle calculation, Ferroelectrics **352**, 148 (2007).

[58] M. DiDomenico and S. H. Wemple, Electrooptical and nonlinear optical properties of crystals, in *Applied Solid State Science*, edited by R. Wolfe (Academic, New York, 1972), Vol. 3, pp. 263–383.

[59] C. Y. Fong, Y. Petroff, S. Kohn, and Y. R. Shen, Wavelength modulation spectra of SbSI and its electronic band structure, Solid State Commun. **14**, 681 (1974).

[60] V. I. Zametin and L. M. Rabkin, Electroreflectance in SbSI, Ferroelectrics **18**, 175 (1978).

[61] K. W. Williams, N. R. Monahan, T. J. S. Evans, and X.-Y. Zhu, Direct Time-Domain View of Auger Recombination in a Semiconductor, Phys. Rev. Lett. **118**, 087402 (2017).

[62] R. Blinc and B. Žekš, *Soft Modes in Ferroelectrics and Antiferroelectrics* (North-Holland, Amsterdam, Oxford, 1974).

[63] L. P. Kadanoff, W. Götze, D. Hamblen, R. Hecht, E. A. S. Lewis, V. v. Palciauskas, M. Rayl, J. Swift, D. Aspnes, and J. Kane, Static phenomena near critical points: Theory and experiment, Rev. Mod. Phys. **39**, 395 (1967).

[64] D. Daranciang, M. J. Highland, H. Wen, S. M. Young, N. C. Brandt, H. Y. Hwang, M. Vattilana, M. Nicoul, F. Quirin, J. Goodfellow *et al.*, Ultrafast Photovoltaic Response in Ferroelectric Nanolayers, Phys. Rev. Lett. **108**, 087601 (2012).

[65] P. S. Bednyakov, B. I. Sturman, T. Sluka, A. K. Tagantsev, and P. V. Yudin, Physics and applications of charged domain walls, Npj Comput. Mater. **4**, 65 (2018).

[66] R. G. P. McQuaid, M. P. Campbell, R. W. Whatmore, A. Kumar, and J. M. Gregg, Injection and controlled motion of conducting domain walls in improper ferroelectric Cu-Cl boracite, Nat. Commun. **8**, 15105 (2017).

[67] T. Sluka, A. K. Tagantsev, P. Bednyakov, and N. Setter, Free-Electron gas at charged domain walls in insulating $BaTiO_3$, Nat. Commun. **4**, 1808 (2013).

[68] M. Schröder, A. Haußmann, A. Thiessen, E. Soergel, T. Woike, and L. M. Eng, Conducting domain walls in lithium niobate single crystals, Adv. Funct. Mater. **22**, 3936 (2012).

[69] R. K. Wehner and E. F. Steigmeier, Coupled lattice modes in light scattering, RCA Rev. **36**, 70 (1975).

[70] T. Schneider and E. Stoll, Observation of Cluster Waves and their Lifetime, Phys. Rev. Lett. **35**, 296 (1975).

[71] M. T. Dove, *Introduction to Lattice Dynamics* (Cambridge University Press, Cambridge, UK, 1993).

[72] J. Grigas and R. Beliackas, Investigations of the central mode in SbSI at microwave frequencies, Ferroelectrics **19**, 113 (1978).

[73] J. Li, L. Zhong, R. Jangid, Meera, G. Rippy, K. Ainslie, C. Kohne, A. S. Everhardt, B. Noheda, Y. Zhang *et al.*, Domain fluctuations in a ferroelectric low-strain $BaTiO_3$ thin film, Phys. Rev. Material **4**, 114409 (2020).

[74] Q. Zhang, E. M. Dufresne, P. Chen, J. Park, M. P. Cosgriff, M. Yusuf, Y. Dong, D. D. Fong, H. Zhou, Z. Cai *et al.*, Thermal Fluctuations of Ferroelectric Nanodomains in a Ferroelectric-Dielectric $PbTiO_3/SrTiO_3$ Superlattice, Phys. Rev. Lett. **118**, 097601 (2017).

[75] R. Z. Tai, K. Namikawa, A. Sawada, M. Kishimoto, M. Tanaka, P. Lu, K. Nagashima, H. Maruyama, and M. Ando, Picosecond View of Microscopic-Scale Polarization Clusters in Paraelectric $BaTiO_3$, Phys. Rev. Lett. **93**, 087601 (2004).

[76] R. Z. Tai, K. Namikawa, M. Kishimoto, M. Tanaka, K. Sukegawa, N. Hasegawa, T. Kawachi, M. Kado, P. Lu, K. Nagashima *et al.*, Picosecond Snapshot of the Speckles from

Ferroelectric $BaTiO_3$ by Means of X-Ray Lasers, Phys. Rev. Lett. **89**, 257602 (2002).

[77] K. Namikawa, M. Kishimoto, K. Nasu, E. Matsushita, R. Z. Tai, K. Sukegawa, H. Yamatani, H. Hasegawa, M. Nishikino, M. Tanaka *et al.*, Direct Observation of the Critical Relaxation of Polarization Clusters in $BaTiO_3$ Using a pulsed x-ray laser technique, Phys. Rev. Lett. **103**, 197401 (2009).

[78] M. Cardona, *Modulation Spectroscopy* (Academic, New York, 1969).

[79] D. Wegkamp, D. Brida, S. Bonora, G. Cerullo, J. Stähler, M. Wolf, and S. Wall, Phase retrieval and compression of low-power white-light pulses, Appl. Phys. Lett. **99**, 101101 (2011).

[80] A. J. Sabbah and D. M. Riffe, Femtosecond pump-probe reflectivity study of silicon carrier dynamics, Phys. Rev. B **66**, 165217 (2002).

[81] N. Ogawa, M. Sotome, Y. Kaneko, M. Ogino, and Y. Tokura, Shift current in the ferroelectric semiconductor SbSI, Phys. Rev. B **96**, 241203(R) (2017).

[82] H. G. Häfele, H. Wachernig, C. Irslinger, R. Grisar, and R. Nitsche, Optical second-harmonic generation in SbSI, Phys. Status Solidi B **42**, 531 (1970).

[83] T. Dekorsy, H. Auer, C. Waschke, H. J. Bakker, H. G. Roskos, H. Kurz, V. Wagner, and P. Grosse, Emission of Submillimeter Electromagnetic Waves BY Coherent Phonons, Phys. Rev. Lett. **74**, 738 (1995).

[84] F. Liu, W. Wu, Y. Bai, S. H. Chae, Q. Li, J. Wang, J. Hone, and X.-Y. Zhu, Disassembling 2D van der waals crystals into macroscopic monolayers and reassembling into artificial lattices, Science **367**, 903 (2020).